49th AIAA Aerospace Sciences Meeting including the New Horizons Forum and Aerospace Exposition
4 - 7 January 2011, Orlando, Florida
AIAA 2011-203
AIAA-2010-0351
49th AIAA Aerospace Sciences Meeting including the New Horizons Forum and Aerospace Exposition.

Numerical Study of Detonation–Turbulence Interaction

L. Massa, M. Chauhan and F.K. Lu,
Mechanical and Aerospace Engineering Department,
University of Texas at Arlington.

A numerical study is performed to investigate the effect of preshock turbulence on the detonation wave properties. The analysis is based on the integration of the chemically reactive Navier–Stokes equations using a Runge–Kutta scheme and a fifth-order WENO spatial discretization. The results show a marked influence of preshock perturbations on the postshock statistics. The alteration to the limit cycle structure supported by unstable waves close to their critical points is highlighted. The effect of reactivity and fluid acceleration in the postshock region are examined by comparison with the non-reactive analog. The possibility that significant forcing can lead to hot spot formation is investigated by considering temperature probability distribution functions in the reaction zone. The separate effect of vortical and entropic fluctuations is considered.

I. Introduction

Many combustion processes are affected by the interaction between turbulence and heat release. In particular, detonation structures interact with a turbulized preshock field both during the initiation[1] and the propagation phases.[2] Possible sources of turbulence ahead of a detonation wave are: turbulent boundary layers resulting from gas dilatation in closed tubes (see Law[3] p. 686), ridges in obstacle laden pipes,[4] shock-flame interactions,[5] and previous (detonation) waves in continuous spin detonation engines.[6]

The detonation–turbulence interaction problem in the present context is concerned with the unsteady coupling between convected vortical/entropic structures and a detonation wave. Acoustic preshock fluctuations, although important to detonation initiation in obstacle-laden pipes (Law[3] p. 686), are not considered in the present study. The dynamics of the interaction reveals the role of preshock fluctuations on the postshock field.

The non-reactive gas analog, shock–turbulence interaction, has been the subject of several theoretical,[7,8] numerical[9–12] and experimental[13,14] investigations. A large portion of past numerical works was concerned with comparing inviscid linear interaction analysis (LIA) with non-linear Navier-Stokes computations. Lee et al.[9] analyzed the non-reactive coupling and found that non-linear computations agree well with Ribner's[7] LIA. While the linear analysis provides useful estimates of the amplification of vorticity fluctuations across the shock, it misses the strong nonlinear dynamics of the energized and highly anisotropic vorticity downstream of the front.

Numerical simulation results presented by Rawat and Zhong[12] indicated that transverse vorticity fluctuations are significantly enhanced across the shock and amplifications increased with the increasing Mach number. Taylor microscales were seen to be reduced just behind the shock after which streamwise microscales rapidly evolve. For turbulent Mach numbers approximately equal to 0.1 the non-linear amplification factor for transverse microscales agrees well with the LIA results.

The detonation–turbulence interaction process differs from the non-reactive shock–turbulence analog because of three reasons: exothermicity, the presence of a length scale associated with the detonation structure, and the presence of natural (intrinsic) fluctuations of the unstable detonation front. Jackson et al.[17] conducted a linear interaction analysis of the reactive problem assuming that the reaction zone thickness is much smaller than the turbulence length scale. They, therefore, neglected both the effect of detonation structure and of intrinsic scales. They concluded that exothermicity affects the interaction of convected isotropic weak

turbulence by amplifying the rms fluctuations downstream of the detonation. The effect of exothermicity is linked to the Mach number, specifically the greatest changes occur around the Chapman-Jouguet condition.

Massa and Lu[18] extended Jackson's analysis by including the effect of the length scale associated with the heat release. They found a strong dependency of the transfer functions on the perturbation wave number through the ratio between fluctuation wavelength and half reaction distance. This phenomenon is absent in shock–turbulence LIA. They showed the existence of resonant wavelengths at which preshock Fourier components are maximally amplified, leading to local maxima in postshock energy spectra. They related the resonant wavelengths with neutral stability conditions (critical points) for the normal mode eigenvalue problem of Short and Stewart.[19] For linearly unstable waves, resonant wave numbers are loci of infinite amplification of postshock power-spectra. Therefore, linear analysis provides useful insights but fails to correctly represent the system dynamics near natural frequencies.

Near the critical point of instability a viscous unstable detonation undergoes Hopf bifurcations to a limit cycle solution. A theoretical proof of the existence of closed orbits for one-dimensional, strong, viscous, detonations was recently devised by Texier and Zumbrun.[20] In a multi-dimensional study, Dou et al.[21] studied the influence of transverse waves on the heat release zone and on the pattern of quasi-steady detonation fronts. They determined that the triple points generated by the motion of transverse waves causes the detonation front to become locally over-driven and form "hot spots" where chemical reaction is enhanced by the coupling of high pressure and high velocity flow. Austin[22] linked the disruption of the regular, periodic, limit cycle structure, and the formation of hot spots in unstable detonations to the mixture effective activation energy.

The present work studies the effect of preshock turbulence on the limit cycle fluctuations. Noise can have a range of effects on an unstable dynamical system, which include stabilization,[23] transition,[24] and resonance.[25] The dynamics of small fluid-mechanics scales is essential to resolving the thermo-fluid interaction in the induction region of a detonation. Both vortical and entropic fluctuations in the preshock field are considered in what is referred to as a forced detonation.

The paper is essentially divided in two parts. The first details the linear interaction analysis (LIA) the second the non-linear forced response.

II. Linearized Perturbation Equations

The linear perturbation equations in the postshock region are obtained from the compressible Euler reactive equations by ignoring second-order contributions and setting the time derivative operator,

$$\frac{\partial}{\partial t} = V\frac{\partial}{\partial y},$$

where $V = u_0 \tan\theta_0$ is the velocity of the steady inertial reference frame defined by Ribner.[16] The perturbation equations are written with respect to a reference system lying on a plane perpendicular to the shock plane and containing the wave number vector $\vec{k}$. In this system, x (without subscript) is the direction normal to the shock and y is the direction parallel to it. The component of the wave number vector on the y axis is $k_y = k\,|\cos(\theta_0)|$. The postshock turbulence components are thus determined in the cylindrical reference system $(x,\ y,\ \phi)$ with associated wave number components $(k_1,\ k_y,\ 0)$. The transverse wave number k_y is unchanged across the shock, while the longitudinal is different from the preshock analog. In the steady reference frame attached to the shock wave, the postshock mean solution features the two flow angles,

$$\theta_1 \equiv \tan^{-1}\left[\tan\theta_0 \frac{M_1^2(\gamma-1)+2}{(\gamma+1)M_1^2}\right],$$

immediately after the shock, and

$$\theta_\infty \equiv \tan^{-1}\left[\frac{\tan\theta_0\left(2+(\gamma-1)M_1^2\right)}{1+\gamma M_1^2-\sqrt{\left(1-M_1^2\right)^2-2Qc_0^2/\gamma\left(\gamma^2-1\right)M_1^2}}\right],$$

in the farfield. Here, M_1 is the Mach number immediately after the shock, which is a function of the preshock Mach number M_0 only, or, by means of a more complex expression, of the detonation structure parameters,

$$M_1^2 = \frac{f(\gamma-1)\left(\gamma Q - Q/\gamma + \sqrt{(\gamma^2-1)\,Q\,(2\gamma+(\gamma^2-1)\,Q)}/\gamma + 1\right)+2}{-\gamma+2f\left(\gamma\left(\gamma Q+\sqrt{(\gamma^2-1)\,Q\,(2\gamma+(\gamma^2-1)\,Q)}/\gamma+1\right)-Q\right)+1}. \tag{1}$$

The solution array is composed by the complex transfer functions,

$$z \equiv [X_\rho, X_u, X_v, X_p, X_\lambda]^T,$$

plus the ratio between the shock front angle and the longitudinal velocity component of the preshock shear wave σ. Denoting by Z the mean-flow solutions,

$$Z \equiv [\rho, u, v, p, \lambda]^T,$$

and changing to a shock-fitting coordinate system,

$$x \to x - \Psi(y,t), \quad \frac{\partial \Psi}{\partial y} = \tan\sigma,$$

we obtain the following vector equation,

$$\boldsymbol{A}\frac{\partial z}{\partial x} + (\boldsymbol{B}+V\boldsymbol{D})\frac{\partial z}{\partial y} + \boldsymbol{C}z - (\boldsymbol{B}+V\boldsymbol{D})\frac{\partial Z}{\partial x}\sigma = 0. \tag{2}$$

The 5×5 matrices denoted with bold typeface are

$$\boldsymbol{A} \equiv \begin{bmatrix} u & \rho & 0 & 0 & 0 \\ 0 & u & 0 & \frac{1}{\gamma\rho} & 0 \\ 0 & 0 & u & 0 & 0 \\ 0 & T-u^2 & 0 & 0 & 0 \\ 0 & 0 & 0 & 0 & u \end{bmatrix}, \quad \boldsymbol{B} \equiv \begin{bmatrix} 0 & 0 & \rho & 0 & 0 \\ 0 & 0 & 0 & 0 & 0 \\ 0 & 0 & 0 & \frac{1}{\gamma\rho} & 0 \\ 0 & 0 & T & 0 & 0 \\ 0 & 0 & 0 & 0 & 0 \end{bmatrix}, \tag{3}$$

$$\boldsymbol{C} \equiv \begin{bmatrix} \frac{\partial u}{\partial x} & \frac{\partial \rho}{\partial x} & 0 & 0 & 0 \\ -\frac{\partial p}{\partial x}/\left(\rho^2\gamma\right) & u & 0 & 0 & 0 \\ 0 & 0 & 0 & 0 & 0 \\ \zeta r_\rho - \frac{T}{\rho}\frac{\partial u}{\partial x} & -2u\frac{\partial u}{\partial x} & 0 & \zeta r_p + \frac{\partial u}{\partial x}/\rho & \zeta r_\lambda \\ -r_\rho & \frac{\partial \lambda}{\partial x} & 0 & -r_p & -r_\lambda \end{bmatrix}, \quad \boldsymbol{D} \equiv \begin{bmatrix} 1 & 0 & 0 & 0 & 0 \\ 0 & 1 & 0 & 0 & 0 \\ 0 & 0 & 1 & 0 & 0 \\ 0 & -u & 0 & \frac{1}{\rho\gamma} & 0 \\ 0 & 0 & 0 & 0 & 1 \end{bmatrix}. \tag{4}$$

where $\zeta = -Qc_0^2(\gamma-1)/\gamma$ and the derivatives of the rate term with respect to density, pressure, and progress variable are:

$$r_\rho = -rE\frac{c_0^2}{p}, \quad r_p = rE\frac{\rho c_0^2}{p^2}, \quad r_\lambda = -K\exp\left(-E\frac{\rho c_0^2}{p}\right). \tag{5}$$

The solution of equation (2) is converted from shock-fitted back to Cartesian coordinates using

$$z \to z - Z_x\Psi(y,t).$$

The evaluation of the auto-correlation in the wave number space, equation (12), and the linearity of the problem allow us to analyze each Fourier component individually, so that the substitution $\partial z/\partial y \to ik_y z$ yields a system of ordinary differential equations in x. The linear system requires six boundary conditions, five are imposed at the shock front, and one at the farfield, $x \to \infty$. The shock boundary conditions are obtained by linearization of the Rankine-Hugoniot shock relations. They are written in vector form as

$$z(\gamma+1) = \boldsymbol{S_a}\frac{\cos\theta_1/\cos\theta_0}{\sqrt{4\cos^2\theta_1\left(1-M_1^2\right)\left(\gamma M_1^2+1\right)+M_1^4(\gamma+1)^2}} + \boldsymbol{S_b}\frac{\tan\theta_1}{M_1^2(\gamma-1)+2}\sigma, \tag{6}$$

where the 5×1 arrays on the right-hand side are defined below,

$$\boldsymbol{S_a} \equiv \begin{bmatrix} 4/M_1\,(1-\gamma) + 8\gamma M_1 \\ \left(M_1^2\left(\gamma^2 - 6\gamma + 1\right) + 4\,(\gamma - 1)\right)\sec\theta_1 \\ 4\left(1 + \gamma\left(2M_1^2 - 1\right)\right)\tan\theta_1 \\ 4\gamma M_1\left(M_1^2\,(\gamma-1) + 2\right) \\ 0 \end{bmatrix}, \tag{7a}$$

$$\boldsymbol{S_b} \equiv \begin{bmatrix} -4\left(1 + \gamma\left(2M_1^2 - 1\right)\right) \\ 2M_1\sec\theta_1\left(M_1^2\left(3\gamma - 1\right) + 3 - \gamma\right) \\ 4/M_1\left(\left(1-2\gamma\right)M_1^4 + (\gamma-3)M_1^2 + \left(\gamma M_1^4 + 1\right)\cos(2\theta_1) + 1\right)\csc(2\theta_1) \\ -4\gamma M_1^2\left(M_1^2\,(\gamma-1) + 2\right) \\ 0 \end{bmatrix}. \tag{7b}$$

The farfield condition is obtained by imposing no left-running characteristics, practically nullifying the upstream traveling acoustic wave. This condition is similar to that proposed by Short and Stewart,[19] but here we include the dependence of the solution on λ. This modified approach reduces the extension of the computational domain in x, and facilitates the task of integrating equation (2) for large wave numbers k_y. In order to do so, we replace in equation (2)

$$\frac{\partial z}{\partial x} \to \alpha z, \quad \frac{\partial z}{\partial y} \to i k_y z,$$

and solve for the α (generalized) eigenvalues and the associated right eigenvectors matrix, $\boldsymbol{R}$. The final condition is obtained by substituting in the eigenvectors matrix the column corresponding to the upstream acoustic with the solution vector $-z$ and imposing that the determinant of such matrix is equal to zero. In a vector form, we write ${\boldsymbol{S_c}}^T z = 0$, where

$$\begin{gathered} \boldsymbol{S_c} \equiv \begin{bmatrix} 0 \\ S_{d2}S_{e5} \\ S_{d3}S_{e5} \\ S_{d4}S_{e5} \\ {\boldsymbol{S_d}}^T\boldsymbol{S_e} \end{bmatrix}, \quad \boldsymbol{S_d} \equiv \begin{bmatrix} 0 \\ V \\ -u \\ i/(\rho\gamma)\sqrt{1 - M_w^2} \\ 0 \end{bmatrix}, \\ \boldsymbol{S_e} \equiv \begin{bmatrix} 0 \\ r_\lambda u\left(-i r_\lambda - k_y V\right)\zeta \\ k_y r_\lambda u^2 \zeta \\ i\zeta r_\lambda^2 u^2 \rho\gamma \\ iT\left(\left(u^2 + V^2\right)k_y^2 + 2i r_\lambda V k_y + r_\lambda^2\left(M_\infty^2 - 1\right)\right) \end{bmatrix}, \end{gathered} \tag{8}$$

and $M_w \equiv \sqrt{\left(u_\infty^2 + V^2\right)/T_\infty}$ and $M_\infty \equiv \sqrt{u_\infty^2/T_\infty} = M_w\cos\theta_\infty$ are the farfield (burnt gas side) Mach numbers in the steady and shock reference frames, respectively. Note: all the flow variables in equation (8) are evaluated in the farfield and the superscript ∞ is dropped for brevity of notation.

II.A. Preshock Turbulence

The preshock turbulence field is assumed to be isotropic, frozen and divergence-free so that the velocity field is obtained as the superimposition of planar vorticity (shear) waves as described in more detail by Ribner.[7] The von Kármán spectral model is used to determine the ratio of the longitudinal velocity spectral density to its mean square value. The von Kármán spectral energy $\mathscr{E}(k)$ decays $\propto k^{-5/3}$ for $k \to \infty$, it ignores the dissipation subrange, and is, therefore, an accurate model for high Reynolds number turbulence.[26] For this reason, the von Kármán model is commonly used in shock–turbulence inviscid LIA.[7,9] In spherical coordinates (k, θ_0, ϕ),

$$\frac{[uu]_0}{\overline{u^2}_0} = \frac{\hat{B}\hat{k}^2\cos^2\theta_0}{2\pi\left(1 + \hat{k}^2\right)^{17/6}}; \tag{9}$$

where,

$$\hat{k} = k\hat{a}L^*,\ \hat{B} = \frac{55}{18\pi\hat{a}},\ \hat{a} = \frac{55}{27\pi}\mathscr{B}\left(1/3, 5/2\right), \tag{10}$$

and $\mathscr{B}$ denotes the Beta function.

II.B. Postshock Turbulence

The amplification of a wave pattern as it goes through the detonation is estimated in terms of auto-correlations. We seek to determine postshock turbulence auto-correlations by integrating the "transferred" wave amplitudes over the preshock wave number space. The evaluation of the transfer functions will be shown in detail in §II. The postshock turbulence is homogeneous on planes parallel to the unperturbed shock front (orthogonal to x_1) and in time. A scalar field $\alpha\left(\vec{x}, t\right)$ is expanded over the (x_2, x_3, t) space in Fourier-Stieltjes series in the general form

$$\alpha\left(\vec{x}, t\right) = \int e^{i[k_2, k_3, k_t]^T [x_2, x_3, t]}\, \mathrm{d}Z_\alpha\left(k_2, k_3, k_t; x_1\right), \tag{11}$$

where k_2 and k_3 are the wave number vector projections onto the respective Cartesian axes, and $k_t = k_1 D_s$, where D_s is the detonation Mach number based on the postshock speed of sound. Considerations about the homogeneity of the scalar field (see, for example, Moyal[27]) lead to expressing the auto-correlation as an integral over the wave number space,

$$\overline{\alpha^2}\left(x_1\right) = \iiint \left[\alpha\alpha\right]\left(k_2, k_3, k_t; x_1\right)\, \mathrm{d}\hat{k}_2\, \mathrm{d}\hat{k}_3\, \mathrm{d}\hat{k}_t; \tag{12}$$

where $[\alpha\alpha]$ is the spectral density over $\left(\hat{k}_2, \hat{k}_3, \hat{k}_t\right)$. The transfer function X_α is defined such that

$$\left[\alpha\alpha\right]\mathrm{d}\hat{k}_2\, \mathrm{d}\hat{k}_3\, \mathrm{d}\hat{k}_t = \left|X_\alpha\right|^2 \left[uu\right]_0\, \mathrm{d}\hat{k}_1\, \mathrm{d}\hat{k}_2\, \mathrm{d}\hat{k}_3, \tag{13}$$

so that integration is performed over the preshock wave number field. Integration over $\hat{k}_2$ and $\hat{k}_3$ defines the one-dimensional power spectrum,

$$\Phi_\alpha\left(\hat{k}_1\right) = \iint \left|X_\alpha\right|^2 \frac{\left[uu\right]_0}{\overline{u^2}_0}\, \mathrm{d}\hat{k}_2\, \mathrm{d}\hat{k}_3. \tag{14}$$

Substitution of equation (9) in equation (14) and conversion from Cartesian to spherical coordinates[7] lead to

$$\Phi_\alpha = \frac{\tilde{B}}{\left|\hat{k}_1\right|^{5/3}} \int \left|X_\alpha\right|^2 \frac{\cos^3\theta_0}{\sin^5\theta_0 \left(\hat{k}_1^{-2} + \sin^{-2}\theta_0\right)^{17/6}}\, \mathrm{d}\theta_0. \tag{15}$$

Note that the power spectra are integrated in $\hat{k}_1 \in [-\infty, \infty]$, the longitudinal wave number in the preshock field.

The transfer function depends on the wave number $\vec{k}$. This is different from the two limiting cases of Jackson et al.[28] and Ribner[7] where it was a function of the angle θ_0 only. The dependence of the transfer function on k highlights the importance of the turbulence scaling effects, here represented by the variable L^*, which were ignored in previous discussions. It will be shown that the eigenvalues of the linear interaction homogeneous problem play a significant role on the dependency of the transfer functions on the wave number.

III. LIA Results

III.A. Activation Energy Effect on Variances and Microscales

For $L^* \to \infty$ the activation energy does not affect the transfer functions (i.e. Jackson et al.'s theory[28]). In this section we seek to identify the effect of E on the turbulence amplification for finite wave thicknesses, and link it to changes in characteristic solutions of the homogeneous problem described in ref.[18] Referring to the stability analysis,[19] we start with a stable detonation structure close to the instability boundary by setting

$Q = 2$, $E = 10$, $\gamma = 1.2$, $f = 1.2$, and $L^* = 1$. The free-stream Mach number $M_0 = 1.9439$ is independent of the activation energy, and will be used for comparison with the non-reactive interaction.

It was shown in ref.[18]that the activation energy plays a significant role on the energy spectra of finite thickness, weakly stable detonations by moving poles of the associated homogeneous problem with respect to the real axis. The emphasis of the present analysis is on the effect of the detonation structure on first order statistics, i.e. autocorrelations and length scales.

Longitudinal compression of fluid particles as they pass through the shock leads to a postshock turbulence with axial symmetry, and decreases both the longitudinal velocity variance $\overline{u^2}$ and the longitudinal Taylor's microscale,[9]

$$\lambda_1 \equiv \sqrt{\frac{\overline{u^2}}{\overline{\left(\frac{\partial u}{\partial x}\right)^2}}}.$$

Both quantities recover immediately after the shock as a result of the decay of the acoustic subcritical contributions to the velocity field. The non-linear analysis of Massa et al.[29] determined that the $\overline{u^2}$ recovery is significantly reduced in reactive conditions, while λ_1 increases faster than in the non-reactive case.

The longitudinal Taylor's microscale is infinite in the von Kármán model because

$$\lim_{k_1\to\infty} \Phi_{u_{x,0}}(k_1) = \lim_{k_1\to\infty} \frac{36k_1^2\Gamma\left(\frac{17}{6}\right)}{55\sqrt{\pi}\left(k_1^2+1\right)^{5/6}\Gamma\left(\frac{1}{3}\right)\left(\tilde{a}L^*\right)^2} \neq 0, \tag{16}$$

where Γ is the gamma function, and the factor $\left(\tilde{a}L^*\right)^2$ is present in the denominator of equation (16) because $L_{1/2}$ is the length scale. Nonetheless, the ratio between preshock and postshock Taylor's microscale is finite, and by using the l'Hôpital's rule

$$\lambda_1 = \sqrt{\frac{\overline{u^2}}{\overline{u^2}_0} \lim_{k_1\to\infty} \frac{\Phi_{u_{x,0}}(k_1)}{\Phi_{u_x}(k_1)}}, \tag{17}$$

where Φ_{u_x} is determined from equation (15) with $X_{u_x} = \partial X_u/\partial x$. The ratio under limit in equation (17) asymptotes to a constant value for $k_1 \to \infty$ and is evaluated at $k_1 = 30$; differences between the values at $k_1 = 30$ and $k_1 = 40$ were found to be negligible.

The longitudinal velocity variance and Taylor's microscale are plotted in the two panels of Fig. 1 for different values of the activation energy, with the non-reactive solution corresponding to Ribner's[7] analysis. The LIA results are consistent with the non-linear analysis. Combustion increases the longitudinal variance immediately after the shock, while the larger postshock Mach number supports a weaker acoustic decay (in agreement with the results of Jackson et al.'s[28]). The longitudinal Taylor's microscale is enhanced by combustion, which selectively energize incoming wavelengths. An increase in activation energy augments the Taylor's microscale effect.

III.B. L^* Effect on a Detonation Close to the Stability Limit

An analysis of the longitudinal velocity variance and microscale for the $L^* \neq 1$ cases is presented in Fig. 2. Close to the shock, the variance of the fluctuation is enhanced by an increase in L^*, while, far from the front, its value is weakly affected. A similar observation holds for the microscale, for which a distinct peak is noted near the half reaction distance ($x = 1$) for large L^*. The weak dependence of the farfield velocity statistics on L^* is not surprising considering the spectra previously shown.[18] Given that the temperature spectra show a more substantial L^* effect, the thermal fluctuation variance is analyzed in the next set of plots.

Experimental observations correlate the presence of hot-spots to non-ideal preshock conditions.[2] The temperature response to incompressible preshock turbulence is here analyzed based on the scaled variance $\overline{T^2}/\overline{u_0^2}$. Results are shown in Fig. 3 for different values of E and L^*. For the reactive cases, a global maximum of $\overline{T^2}$ is present within the reaction zone. This peak is pronounced and increases in magnitude with both E and L^*, signaling the propensity for hot spot formation for higher activation energies and longitudinal scale of turbulence. The relationship between temperature amplification and E is consistent with Austin's[22] experimental observations on hot spot formation. Note that Austin did not consider a turbulent inflow, and the postshock fluctuations were result of intrinsic instability; yet the experiments link spikes in temperature disturbances within the reaction zone to the activation energy.

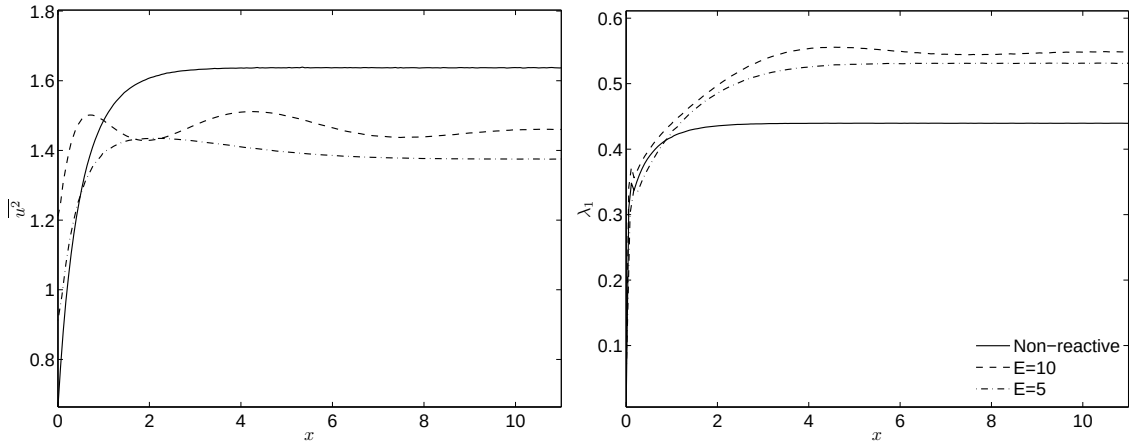

(a) Variance (b) Microscale

Figure 1. Longitudinal velocity variance and Taylor's microscale for $Q = 2$, $E = 5,\ 10$, $\gamma = 1.2$, $f = 1.2$, and $L^* = 1$ ($M_0 = 1.9439$).

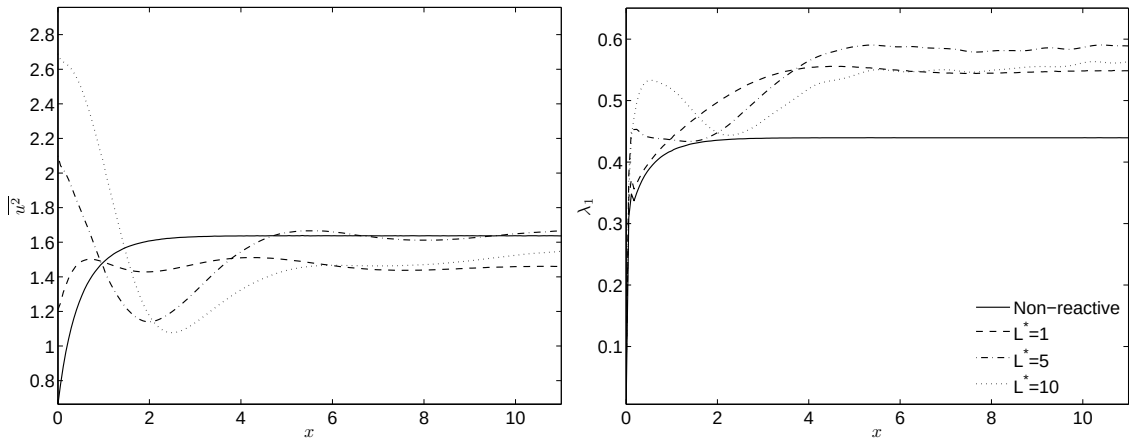

(a) Variance (b) Microscale

Figure 2. Longitudinal velocity variance and Taylor's microscale for $Q = 2$, $E = 10$, $\gamma = 1.2$, $f = 1.2$, and $L^* = 1,\ 5,\ 10$ ($M_0 = 1.9439$).

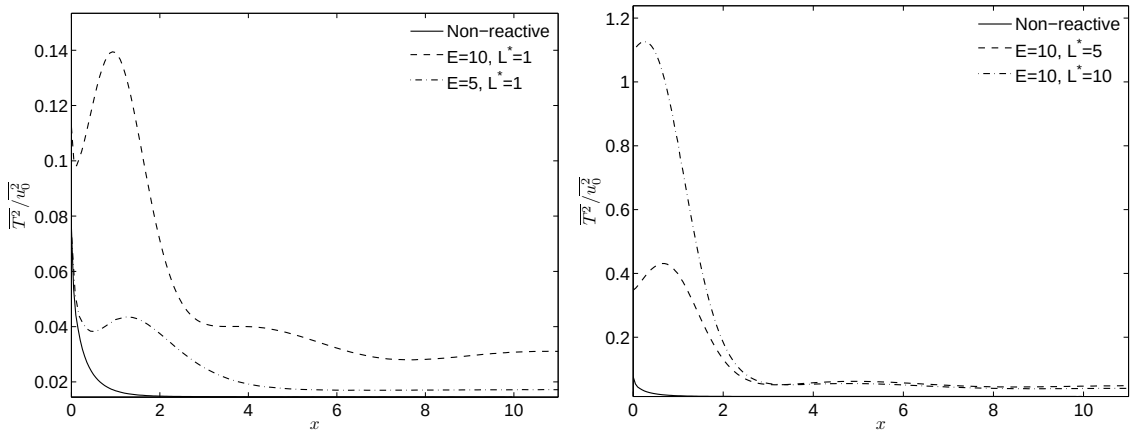

(a) Variance (b) Microscale

Figure 3. Scaled temperature variance for $Q = 2$, $E = 5,\ 10$, $\gamma = 1.2$, $f = 1.2$, and $L^* = 1,\ 5,\ 10$ ($M_0 = 1.9439$).

IV. Non-Linear Analysis, Governing Equations

IV.A. Scales

The scales for the detonation–turbulence interaction problem are the root mean square of the longitudinal velocity at the inflow $u_{rms,0}$, the inflow Taylor microscale λ_0 based on the dissipation function, the preshock unperturbed density ρ_0, and the specific gas constant R. This choice of scales is maintained for zero inflow turbulence, the condition referred to as non-forced or natural detonation, by using the scales for the corresponding forced case.

When performing linear analysis of detonation instability, the growth rate eigenvalue and associated eigenfunctions are reported with a slightly different choice of scales. In such a case, the half detonation distance $L_{1/2}$ and the preshock pressure p_0 are used in place of λ_0 and $u_{rms,0}$. To avoid confusion, the scaling will be explicitly mentioned in the linear growth analysis.

IV.B. Navier–Stokes Equations

The governing equations are the non-dimensional conservative form of the continuity, momentum and energy equations in Cartesian coordinates. The working fluid is assumed to be a perfect gas.

$$\frac{\partial \rho}{\partial t} + \frac{\partial}{\partial x_j}(\rho u_j) = 0 \tag{18a}$$

$$\frac{\partial}{\partial t}(\rho u_i) + \frac{\partial}{\partial x_j}(\rho u_i u_j + p\delta_{ij} - \sigma_{ij}) = 0, \quad i = 1, 2, 3 \tag{18b}$$

$$\frac{\partial E_t}{\partial t} + \frac{\partial}{\partial x_j}(E_t u_j + u_j p + q_j - u_i \sigma_{ij}) = 0 \tag{18c}$$

$$\frac{\partial \rho\lambda}{\partial t} + \frac{\partial(\rho\lambda u_j + \rho J_j)}{\partial x_j} = (\rho - \rho\lambda) r(T), \tag{18d}$$

where the viscous stress tensor, heat flux vector, and the mass diffusion velocity are

$$\sigma = \frac{\mu}{Re}\left(\boldsymbol{\nabla}\vec{u} + \boldsymbol{\nabla}\vec{u}^T - \frac{2}{3} I_{3,3} \boldsymbol{\nabla}\cdot\vec{u}\right), \tag{19a}$$

$$\vec{q} = -\frac{\gamma}{\gamma - 1}\frac{\mu}{RePr}\boldsymbol{\nabla} T, \tag{19b}$$

$$\rho\vec{J} = -\frac{\mu}{RePrLe}\boldsymbol{\nabla}\lambda \tag{19c}$$

$$\mu = \left(\frac{T}{T_0}\right)^{0.7}, \tag{19d}$$

where $I_{3,3}$ is the 3×3 identity matrix. The variable λ is the reaction progress, where $\lambda = 0$ describes the unburnt state and $\lambda = 1$ the completely burnt state. The total energy of the fluid is given by

$$E_t = \rho\left(\frac{P}{\gamma - 1} + \frac{u_i^2}{2} - \tilde{Q}\lambda\right) \tag{20}$$

where $\tilde{Q}$ is the non-dimensional heat release so that the term $\tilde{Q}\rho\lambda$ denotes the non-dimensional chemical energy released as heat during the burning process. The reaction rate $r(T)$ is described by a single step mechanism, where the Arrhenius law depends on temperature T through the relation

$$r(T) = K_0 \exp\left(-\frac{\tilde{E}}{T}\right) \tag{21}$$

where K_0 is the pre-exponential factor that sets the temporal scale of the reaction, $\tilde{E}$ is the non-dimensional activation energy.

V. Numerical Set-up

A sketch of the computational set-up for the study of turbulence detonation interaction is shown in Fig. 4. The domain is three-dimensional with a square transverse section $(x - z)$ and periodic boundary conditions at the $x - y$ and $x - z$ planes. Non-reflective boundary conditions are implemented at the subsonic out-flow boundary. The conditions at the supersonic inflow are detailed in §VI.A.

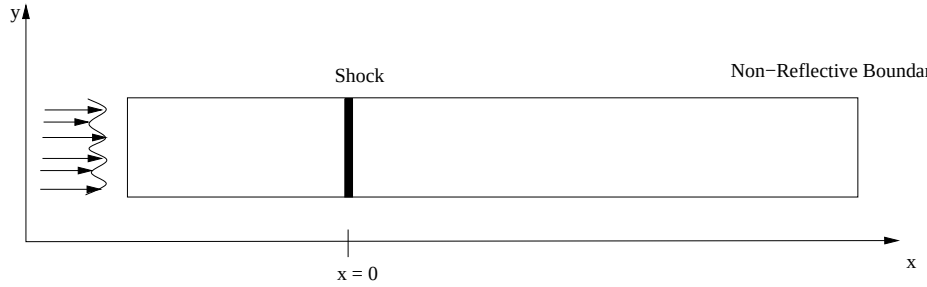

Figure 4. Sketch of the computational set-up.

VI. Test Cases

Consider a one–dimensional detonation structure with unit overdrive $f = 1$ and constant isentropic index γ, there is a one-to-one relationship between inflow Mach number in shock reference frame M and heat release parameter,

$$Q \equiv \frac{\tilde{Q}}{p_0/\rho_0} = \frac{\tilde{Q}}{\gamma M_t^2} = \frac{\gamma\left(M^2 - 1\right)^2}{2\left(\gamma^2 - 1\right)M^2}, \tag{22}$$

with M_t the turbulent Mach number. Note that Q is purely a detonation parameter and is independent of the inflow turbulence, while $\tilde{Q}$ is an interaction parameter and depends on the inflow turbulence through M_t. Therefore, a one-dimensional detonation structure with unit overdrive can be identified by assigning M, $E \equiv \tilde{E}/\left(p_0/\rho_0\right)$ and γ.

In all cases considered, the isentropic index is kept fixed and equal to $\gamma = 1.2$. Two free-stream Mach number conditions are considered in the present research. The low heat release case features $M = 4.0$ and, thus, $Q = 19.18$. The high heat release case has $M = 5.5$, which gives $Q = 38.57$.

The activation energy E can be physically related to responsive changes in induction time with the postshock temperature in von Neumann conditions, $(\partial \ln \tau_i / \partial \ln T_{ps})_{f=1}$, where τ_i is the induction time and T_{ps} is the postshock temperature.[30] The choice of activation energy in the present study has been primarily dictated by selecting detonation structures that are longitudinally stable, i.e. , stable to one-dimensional perturbations. Longitudinal instability gives rise to axial motion of the mean shock front and galloping waves,[20] which complicates the evaluation of the ensemble average as a time-space mean at a fixed normal-to-the shock distance. The longitudinal instability boundary divides the $E-Q$ quarter plane in two convex regions. Such a boundary for $\gamma = 1.2$ and unit overdrive is shown in the bottom panel Fig. 5. Based on this figure, the choices $E = 12$ and $E = 20$ are made for low ($Q = 19.18$) and high ($Q = 38.57$) heat release cases, respectively. The high heat release conditions are similar to those used by Dou et al.[21] who simulated a detonation wave with $Q = 50,\ E = 20,\ \gamma = 1.2$ and $f = 1$.

Dissipation effects lead to the definition of the Reynolds number Re_λ which will be set based on the decay of homogeneous isotropic turbulence described in §VI.A, the Prandtl and Lewis numbers, which are fixed to $Pr = 0.72$ and $Le = 1$. Compressibility effects in the incoming turbulent flow are set by assigning the turbulent Mach number $M_t \equiv u_{rms}/\sqrt{\gamma p_0/\rho_0}$, which leads to the determination of the mean preshock pressure p_0. The value of M_t is discussed in §VI.A. The final model parameter K_0 is assigned by imposing the half reaction distance $L_{1/2}$ through the ratio $L^* = L_{1/2}/\lambda_0$, where L^* represents a ratio of detonation to turbulent scales and is set equal to one in all test cases.

Note that the Reynolds number based on acoustic velocity and half reaction distance, $Re_{L_{1/2}} \equiv \sqrt{p_0\rho_0}L_{1/2}/\mu_0 = Re_\lambda L^*/\left(\sqrt{\gamma}M_t\right)$, is quite small in the simulations presented. In fact, for $L^* = 1$, typical values of $M_t \approx 0.2$ and Re_λ small enough to allow for a direct numerical simulation (DNS) of the problem, $Re_{L_{1/2}} \approx 200$. An increase in L^* leads to a proportional increase in $Re_{L_{1/2}}$, but also to a similar increase in domain size and computational requirements. Therefore, for practical reasons, the DNS presented here refer to a very thin detonation wave with, in practice, a sub-millimeter reaction distance. The influence of a small Reynolds number on the growth rate of normal mode disturbances is analyzed in.[29]

Three simulations at low heat release are discussed, a reactive, a non-reactive and a non-forced one. The non-reactive corresponds to shock–turbulence interaction conditions, with free-stream Mach number $M = 4.0$. The non-forced conditions are obtained by zeroing out the incoming turbulence so that only natural instability fluctuations are present in the postshock field. Similarly, three simulations at high heat release are considered. In this case, two different kinds of inflow turbulence are analyzed together with the non-forced detonation. The first forced inflow case has only vortical waves, obtained from the decay of homogeneous turbulence described in §VI.A. In the second case, the vortical waves are nullified in favor of entropy waves obtained using the Morkovin[31] scaling: an empirical relationship between temperature and longitudinal velocity perturbation valid in constant pressure boundary layers. Density fluctuations in the constant pressure inflow are related to the isotropic turbulence velocity perturbation by

$$\rho'/\bar{\rho} = (\gamma - 1)M^2 \frac{u'}{\bar{u}}. \tag{23}$$

Mahesh et al.[32] used equation (23) to analyze the influence of entropy perturbation on the shock–turbulence interaction, and discovered a strong influence of preshock density fluctuations on postshock perturbation dynamics.

VI.A. Inflow Boundary Conditions and Temporal Decay

The inflow boundary conditions are implemented by imposing the fluid state on the supersonic inflow side. The procedure is similar to that described by Mahesh et al.[32] The flow is decomposed into a mean and perturbation part. The perturbation is evaluated by temporal decay of homogeneous, isotropic, compressible turbulence in a cube with periodic boundary conditions. The initial spectrum is Gaussian and symmetric with kinetic energy density

$$\mathscr{E}(k) = \frac{16\sqrt{\frac{2}{\pi}}\exp\left(-\frac{2k^2}{k_0^2}\right)k^4}{k_0^5}, \tag{24}$$

with $k_0 = 3$.

The spatial realization used to model the inflow boundary conditions corresponds to the $t = 3$ solution, for which the inflow turbulent Mach number is $M_t = 0.235$. The time-decayed turbulence is rescaled so that

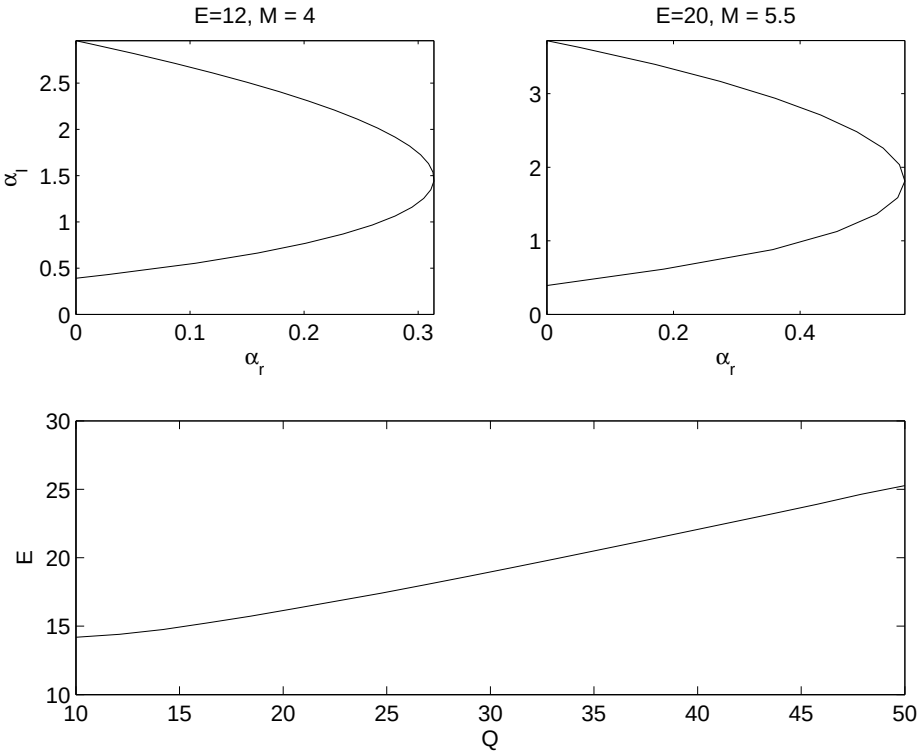

Figure 5. Normal mode analysis of detonation instability. Top two panels: real and imaginary part of the eigenvalue. Bottom panel, longitudinal instability boundary for $\gamma = 1.2$ and unit overdrive.

the length and velocity scales are the Taylor micro-scale λ and the velocity rms for the spatial realization at $t = 3$. The detonation–turbulence interaction is carried out by advecting the random spatial realization, thus assuming frozen dynamics. Lee et al.[15] have shown that Taylor's hypothesis is valid for a wide range of compressible flows that includes the present conditions. The present M_t value is large compared to similar studies, e.g. Lee et al.,[9] because the stability of the limit cycles renders the contribution of small noise marginal with respect to the natural fluctuations.

VII. Non-linear Analysis Results

VII.A. Energy Spectra

One-dimensional spectra for the longitudinal velocity Φ_u in the postshock field are determined as functions of the temporal wave number k_t by calculating the Fourier transform of space–time sequences $u'(t, y, z)$, and summing the three dimensional spectral density function $\hat{u}(k_t, k_y, k_z) \equiv \mathscr{F}(u'(t, y, z))\,\mathscr{F}(u'(t, y, z))^*$ over the spatial wave numbers k_y and k_z. These temporal spectra are identical to spatial averages over planes perpendicular to the mean flow of the spectra of time sequences taken at fixed spatial locations. The one-dimensional spectra are normalized so that the sum of their values at the discrete wave numbers at which they are evaluated is equal to the variance of the fluctuation.

Energy spectra at four distances from the shock are shown in Fig. 6 for reactive and non-reactive conditions, in the low heat release case. The thick dashed line has slope $\propto k_t^{-5/3}$ and, by assuming Taylor's hypothesis, indicates the inertial sub-range. The significant difference between shock–turbulence and detonation–turbulence interaction is evident by comparing the two panels of Fig. 6. A pronounced peak characterizes the response of a detonation to turbulence, and leads to the identification of a characteristic frequency of maximal spectral density, in good agreement with linear analysis predictions.[18] A comparison between forced and non-forced spectra presented in the first row of Fig. 7 reveals that such a characteristic frequency is associated with natural fluctuations. The figure shows that in the forced case the majority of the fluctuation kinetic energy is associated with limit cycle oscillations. Nonetheless, the peaks of the spectrum

are smoothed and decreased in magnitude by the addition of inflow turbulence.

A similar result is obtained by comparing forced and non-forced high heat release cases. The results are shown in the second and third rows of Fig. 7 for vortical and entropy waves respectively. The peak frequency is approximately constant when changing the distance from the shock and matches the frequency of the most amplified linear wavelength as inferred from the top panels of Fig. 5. Due to the different non-dimensionalization used in the growth rate eigenvalue computations, α values in Fig. 5 must be multiplied by $\left(M_t\sqrt{\gamma}\right)^{-1}$ to compare with the turbulent computations. After conversion to the inflow fluctuation scales, the most amplified linear frequencies are 5.6 and 6.98 for the low and high heat release cases, respectively. The peak in response spectra are at $k_t = 5.2$ and 6.91, for the analogous non-linear cases.

The two bottom rows of Fig. 7 also reveal that the entropy fluctuations are more effective in disrupting the periodic limit cycle solutions supported by the intrinsic detonation instability. The difference between forced and non-forced cases is much larger in the bottom row of Fig. 7 than in the middle one.

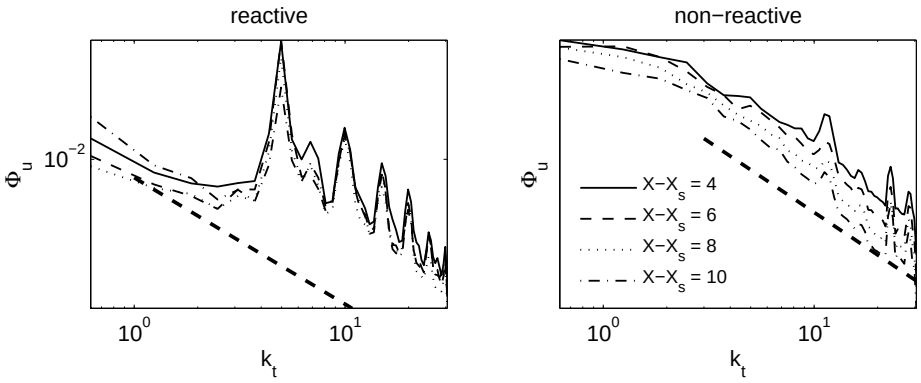

Figure 6. One–dimensional energy spectra against temporal wave number. Comparison of reactive and non-reactive cases with vortical inflow at $M = 4$. The thick dashed line is $\propto k_t^{-5/3}$.

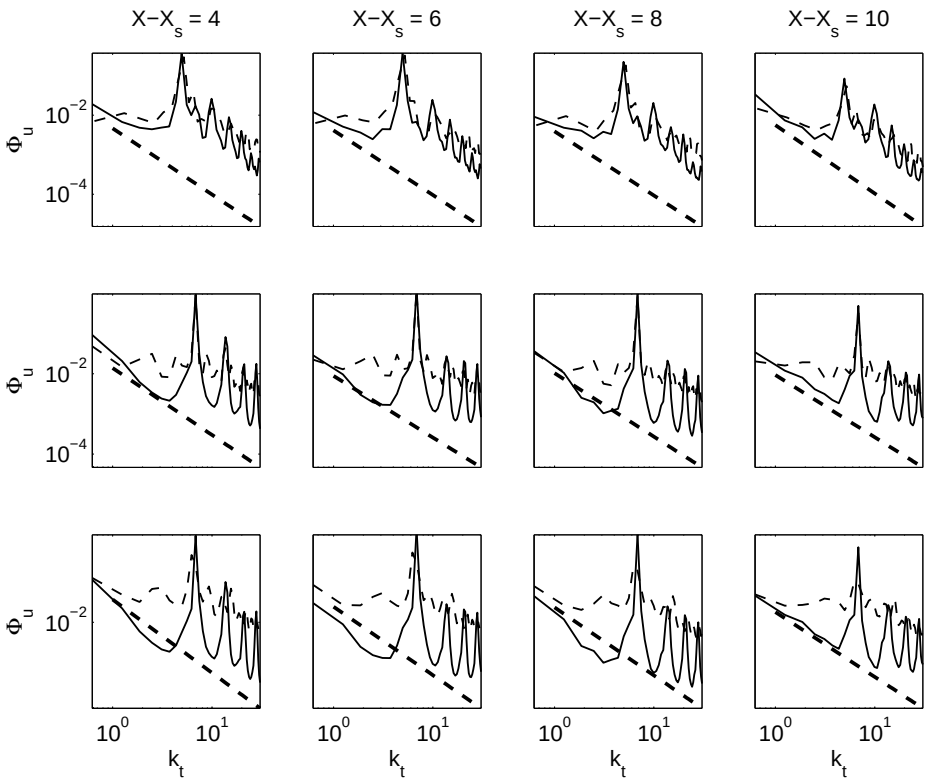

Figure 7. One–dimensional energy spectra against temporal wave number: comparison of forced and non-forced cases. Each column represents a distance from the shock as indicated in the column titles. Top row, low heat release, $M = 4$; solid line non-forced and dashed line vortical forcing. Mid row, high heat release, $M = 5.5$; solid line non-forced and dashed line vortical forcing. Bottom row, high heat release, $M = 5.5$; solid line non-forced and dashed line entropic forcing. In all panels, the thick dashed lines are $\propto k_t^{-5/3}$.

VII.B. Analysis of Variances and Auto-correlations

The forced and non-forced spectra presented in §VII.A reveal marked differences in the responses of reactive and nonreactive configurations to a turbulent inflow. Such differences are investigated in more detail by analyzing variances of the fluctuation where, as before, ensemble averages are computed as space–time averages at constant distance from the shock. In general, the use of so-called Favre averages (see, for example, Warsi[33] p. 481), used for example by Lee,[9] changes the results only marginally, therefore non-weighted averages are used in all results presented in this work.

The meanflow structure is significantly affected by intrinsic and forced fluctuations. Figure 8 shows the mean temperature and velocity for the five reactive cases along with the corresponding unperturbed Zel'dovich-Neumann-Doering (ZND) profiles. For all cases, the jump across the shock is lower than that predicted by the Rankine–Hugoniot conditions. This phenomenon is a consequence of both shock front motion and corrugation, and is consistent with the mean shock profiles reported by Lele and Larson[34] at large M_t and in non-reactive conditions. The reaction length supported by turbulent inflow $\overline{L_{1/2}}$ is evaluated based on the mean profile as the distance between the location at which $\overline{\lambda} = 1 \times 10^{-3}$ and that at which $\overline{\lambda} = 0.5$. For the low heat release condition, the non-forced and vorticity forced cases have $\overline{L_{1/2}}$ equal to 1.840 and 1.542 respectively. For the high heat release condition, the non-forced, vorticity forced and entropy forced cases have $\overline{L_{1/2}}$ equal to 1.963, 1.889 and 2.312 respectively. The intermittent corrugation of the front expands the half reaction distance above the one-dimensional value of $L_{1/2} = 1$. Vorticity forcing ahead of the wave tends to reduce the region of heat release, with a more pronounced effect in low heat release conditions, while entropy forcing leads to an increase in $\overline{L_{1/2}}$.

Longitudinal and transverse velocity variances are shown for the six cases in Fig. 9. The top-row panels refer to the low heat release case and the solid, dashed and dotted curves represent non-reactive, non-forced and vortical inflow solutions respectively. The major difference between shock–turbulence and detonation–

turbulence interaction is the loss of the longitudinal fluctuation peak immediately after the shock. Such a local maximum is due to the decay of sub-critical acoustic waves (those which are damped in the postshock far-field) followed by viscous dissipation, and is typical of non-reactive conditions as the linear interaction analysis of Rawat and Zhong[12] shows. Moreover, for the reactive cases, the presence of inflow vortical fluctuations increases transverse fluctuations of up to 50% above the non-forced values, at selected locations.

Note in top-left panel of Fig. 9 that the non-reactive longitudinal correlation immediately after the shock is larger than its preshock value. This behavior is in contrast with that reported in literature.[9,12] Further analysis shows that this result is a consequence of the high turbulent Mach number, and is associated to the large shock corrugation. In Fig. 10, such longitudinal variances are compared to a non-reactive $M_t = 0.1$ case. The comparison shows that the low M_t case behaves similarly to literature data.[9,12] Moreover, the $M_t = 0.235$ variance presents a much higher peak immediately after the shock, and drops below the low M_t case far from the front.

The two bottom panels of Fig. 9 refer to the high heat release case with solid, dashed and dotted lines indicating non–forced, vortical and entropy wave solutions, respectively. Vortical fluctuations produce a weaker increase in transverse variances in the high heat release case than in the low heat analog. It is also evident that the limit cycles are less sensitive to vorticity forcing than to entropy forcing. The inflow entropy fluctuation is more effective than the vortical analog in reducing the longitudinal velocity fluctuations associated with the detonation instability. Contrary to vorticity forcing, the addition of entropy forcing reduces postshock transverse fluctuations.

To provide a graphical analysis of the effects of turbulence on detonations, numerical schlieren snapshots are shown in Figs. 11–13 for the three high heat release cases. All panels refer to an $x - y$ slice at half the box size, $z = L/2$. Each panel represents a different time as indicated in the titles. The time sequence covers approximately the period of the most amplified linear mode $T_\alpha = 2\pi/6.98 \approx 0.9$, which was previously shown to match the wave number of the maximum of the velocity spectra. The non-forced case shows a time periodicity typical of limit cycle solutions. Both forced cases display a more complex time history. A considerably more perturbed postshock field is noticed in the entropy forced case, where large pockets of high density material detach from the shock front and are convected downstream. These regions correspond with unburned material convected through the reaction region. Temperature fluctuations in the fire zone are amplified by the perturbed inflow (a more detailed analysis is presented in §VII.C), but no evidence of hot spots is found.

Auto-correlations in planes parallel to the unperturbed shock front are presented in terms of integral length scales. The scales are evaluated by integrating the correlation coefficient built on space–time averages against the separation distance. The autocorrelation coefficient is a scaled two–point correlation function, so that the integral length associated to a general variable f takes the form,

$$\Lambda_f = \frac{\int_0^{L_2} \overline{f\left(x,y,z,t\right)' f\left(x,y+h,z,t\right)'}\,\mathrm{d}h}{\sigma_f}, \tag{25}$$

where σ is the variance. Davidson[35] explained that autocorrelation helps in differentiating between the small and large scale eddies in turbulence, and is preferable to one–dimensional, scalar functions, such as u_x. It is conventional to evaluate the Fourier transform of the velocity correlation tensor Q_{ij} with diagonal components Q_{ii} representing autocorrelation functions for the velocity components u_i. Huang et al.[36] argued that the autocorrelation function is a good indicator of the inertial sub-range.

Temperature, longitudinal velocity, density and progress of reaction (Λ_T, Λ_u, Λ_ρ, and Λ_λ) scales are plotted against the distance from the shock in the four panels of Figs. 14–15. The two figures show the strong effect of natural detonation fluctuations in increasing the integral scales across the shocks. The addition of inflow turbulence breaks natural scales and considerably reduces the integral scale. Entropy inflow perturbations are found to be more effective than vorticity analogs in breaking regular structures.

Longitudinal velocity and transverse velocity Taylor microscales, λ_1 and λ_2 are plotted in Fig. 16 for the two levels of heat release. The Taylor microscales are evaluated as

$$\lambda_1 = \sqrt{\frac{\overline{u'^2}}{\overline{\left(\frac{\partial u'}{\partial x}\right)^2}}}, \quad \lambda_2 = \sqrt{\frac{\overline{v'^2}}{\overline{\left(\frac{\partial v'}{\partial y}\right)^2}}}. \tag{26}$$

They are strongly affected by the reactivity of the mixture in the postshock field. The detonation–turbulence interaction supports significantly higher values of the microscale than the nonreactive analog. Nevertheless,

the distribution of the microscale in the postshock field is not significantly affected by an increase in heat release. The addition of a turbulent inflow has also a marginal effect on the microscale. This conclusion is in contrast with that drawn for the integral scale. The longitudinal microscale for the reactive cases is significantly larger than the transverse one, showing the effect of combustion in energizing (accelerating) longitudinal structures at selective wave numbers. The selectivity of the reactive interaction is in agreement with the results of linear analysis,[18] and the presence of local maxima in the post shock spectra shown in §VII.A. Entropy fluctuations behaving according to Morkovin's hypothesis are more effective in reducing the microscale in the postshock field than the vortical analogs.

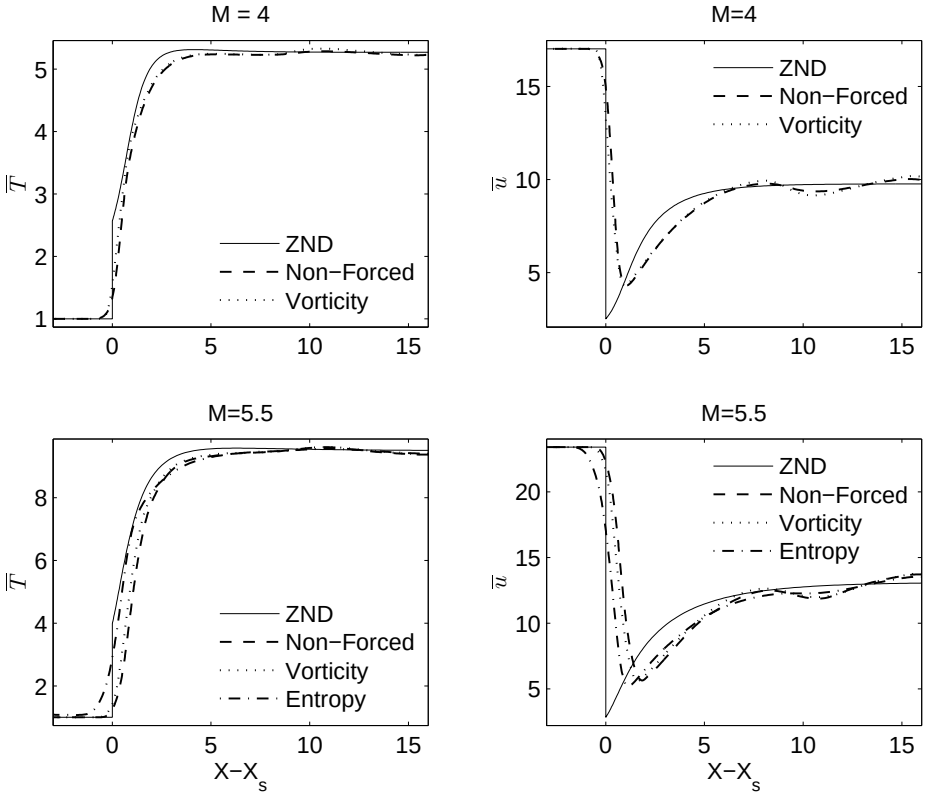

Figure 8. Temperature and longitudinal velocity means for the five reactive cases. ZND profiles refer to the classical one-dimensional, steady analysis of detonation waves.

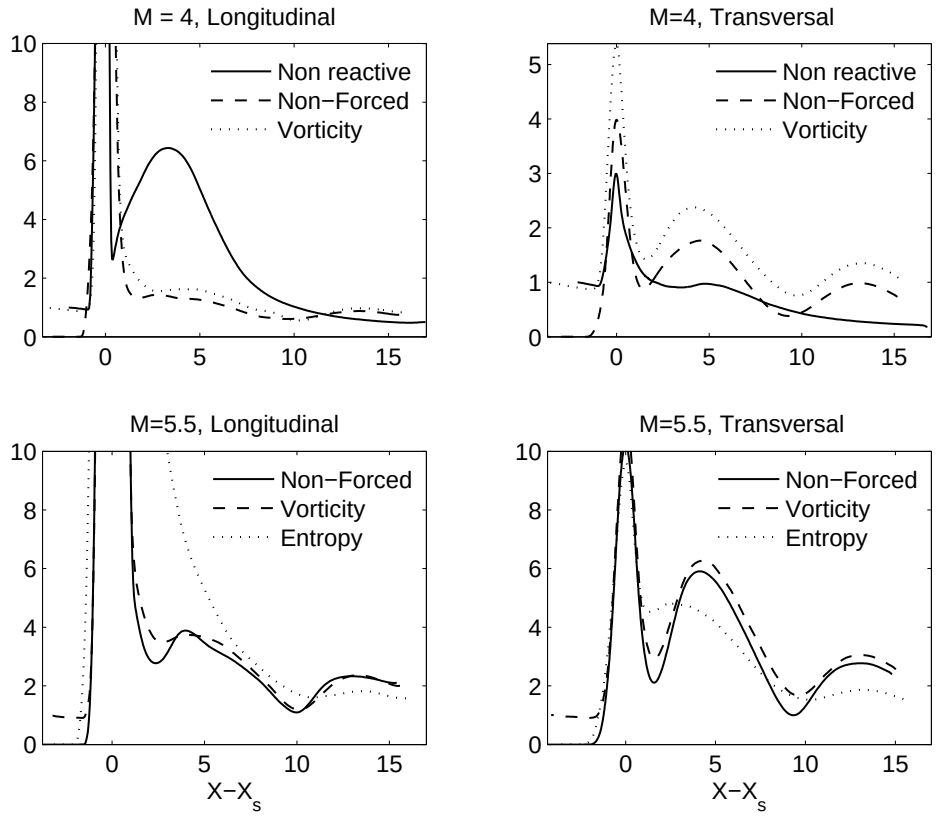

Figure 9. Longitudinal and transverse velocity variances for different inflow forcing and Mach numbers.

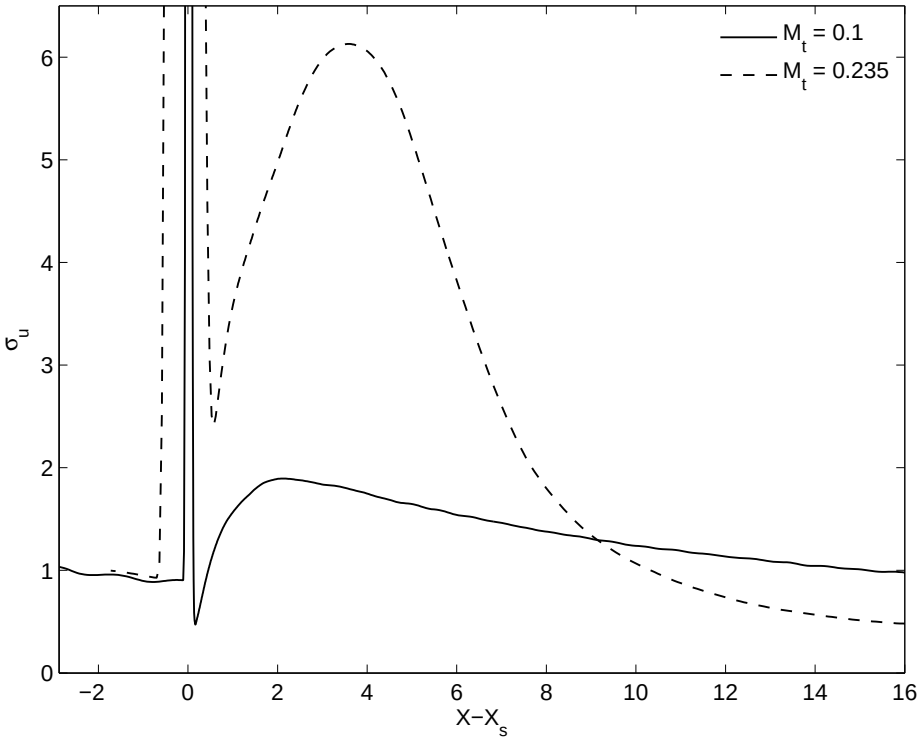

Figure 10. Comparison of low and high M_t non-reactive cases variances at $M = 4$.

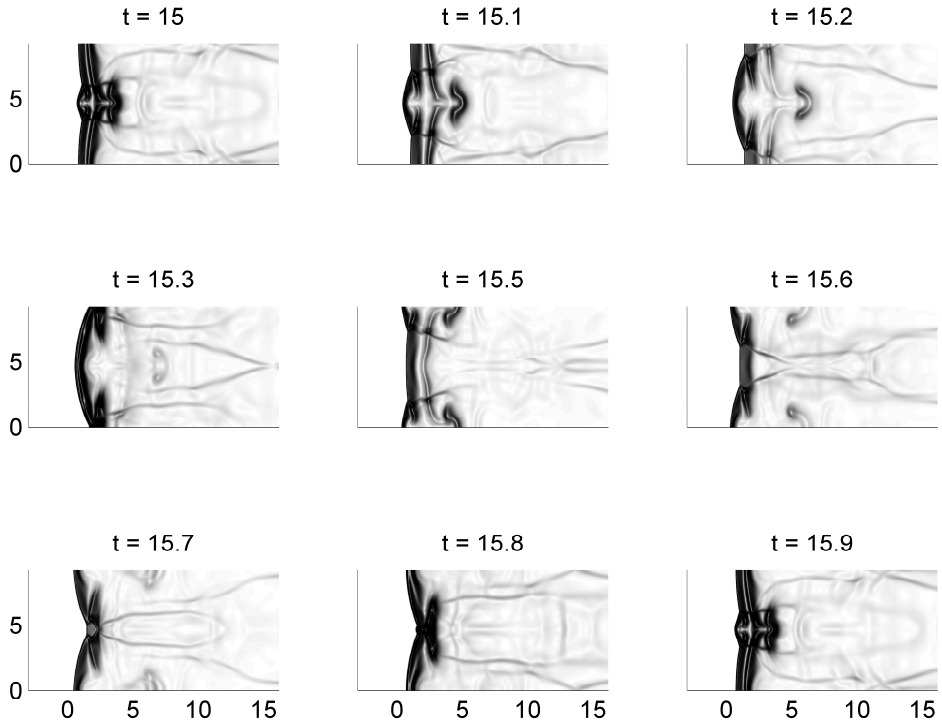

Figure 11. Numerical schlieren for the non-forced $M = 5.5$ case. Different panels refer to the same $z = L/2$ slice but different times, as indicated on top of each panel. The time-interval $15.0 - 15.9$ corresponds with the period of the most amplified normal mode $T_\alpha = 2\pi/6.98 \approx 0.9$.

VII.C. Probability Distribution Functions

A set of probability distribution functions (PDF) is evaluated in the post-shock region by determining conditional probabilities for $\lambda < 0.5$ and $p > p_{\text{ZND}}/2$, where p_{ZND} is the maximum pressure for a steady detonation wave. The conditional probability functions for longitudinal velocity and temperature are plotted for all cases in Fig. 17. For both heat release cases, the response to vortical forcing leads to a larger range of fluctuations. The changes in both u and T fluctuations are substantial in the near-shock region. Entropy fluctuations support stronger changes than vortical fluctuations. The temperature PDF for the entropy forcing case manifests a significant increase at large temperatures, which points to the possibility of supporting hot spot formation at higher activation energies.

Changes in fluctuations caused by the turbulent inflow decrease downstream of the shock plane, as demonstrated by longitudinal velocity PDFs evaluated at different downstream locations (x = constant) shown in Figs. 18 and 19. The marked difference between reactive and non reactive longitudinal velocity PDF shown in Fig. 18 is due to gas acceleration caused by the reactivity. The temperature PDF (not shown) behaves similarly to the velocity counterpart: differences caused by the forcing quickly diminish as the distance from the shock is increased, leading to a downstream PDF that is weakly dependent on the inflow perturbation.

VIII. Conclusions and Future Work

The present research examines the interaction of turbulence with a detonation wave from both the linear and non-linear standpoints. The focus is on changes with respect to the shock–turbulence analog as a consequence of the reactivity. Nonlinear calculations are carried out to investigate modifications to the limit-cycle natural fluctuations caused by strongly perturbed inflows. Linear interaction analysis is limited to weakly stable (i.e. close to the stability boundary) conditions, and explains the role of system natural frequencies on first order statistics.

The main conclusions of the present work are summarized below. For a turbulent Mach number $M_t =$

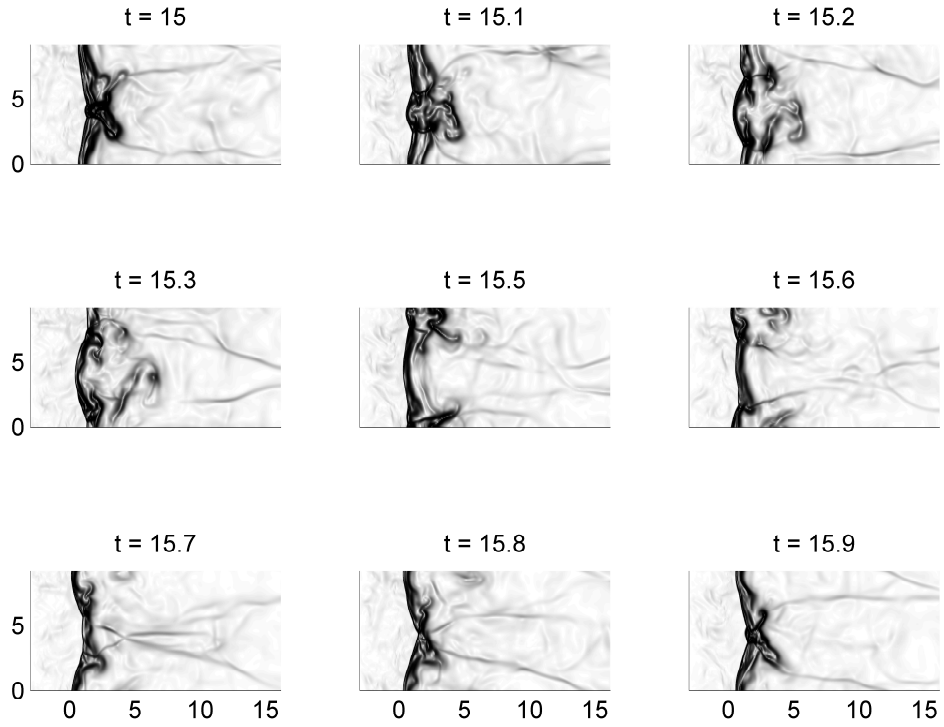

Figure 12. Numerical schlieren for the vorticity perturbation $M = 5.5$ case. Different panels refer to the same $z = L/2$ slice but different times, as indicated on top of each panel.

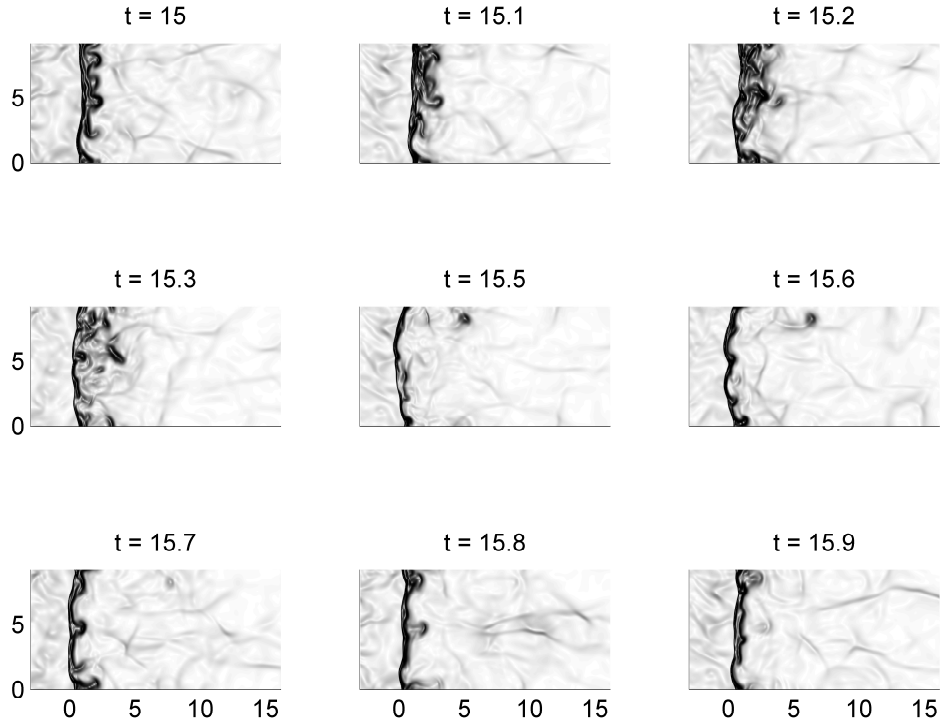

Figure 13. Numerical schlieren for the entropy perturbation $M = 5.5$ case. Different panels refer to the same $z = L/2$ slice but different times, as indicated on top of each panel.

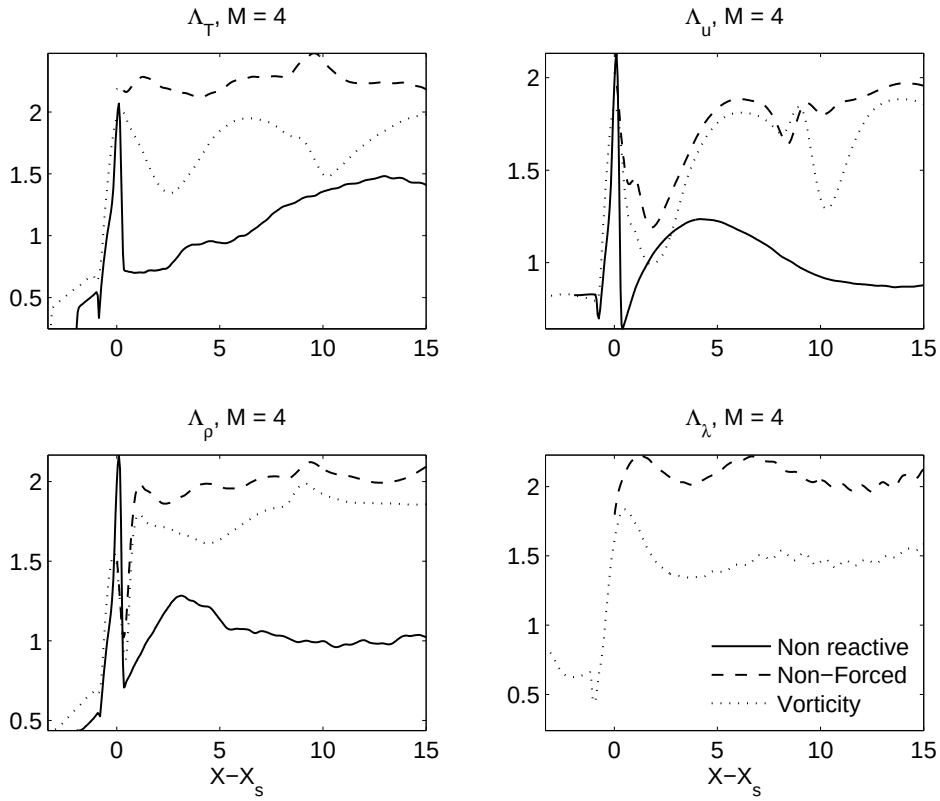

Figure 14. Comparison of integral length scales for the low heat release case. The legend shown in the bottom-right panel applies to all. In the bottom right panel, the non-reactive curve is not drawn because the progress of reaction is not defined.

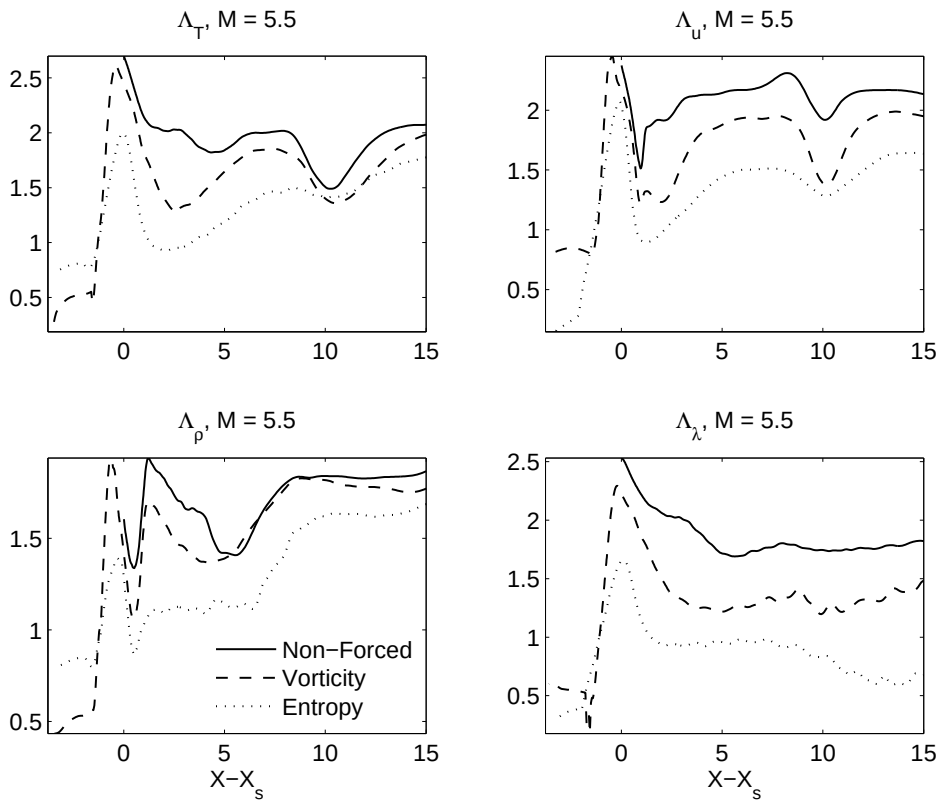

Figure 15. Comparison of integral length scales for the high heat release case. The legend shown in the bottom-left panel applies to all.

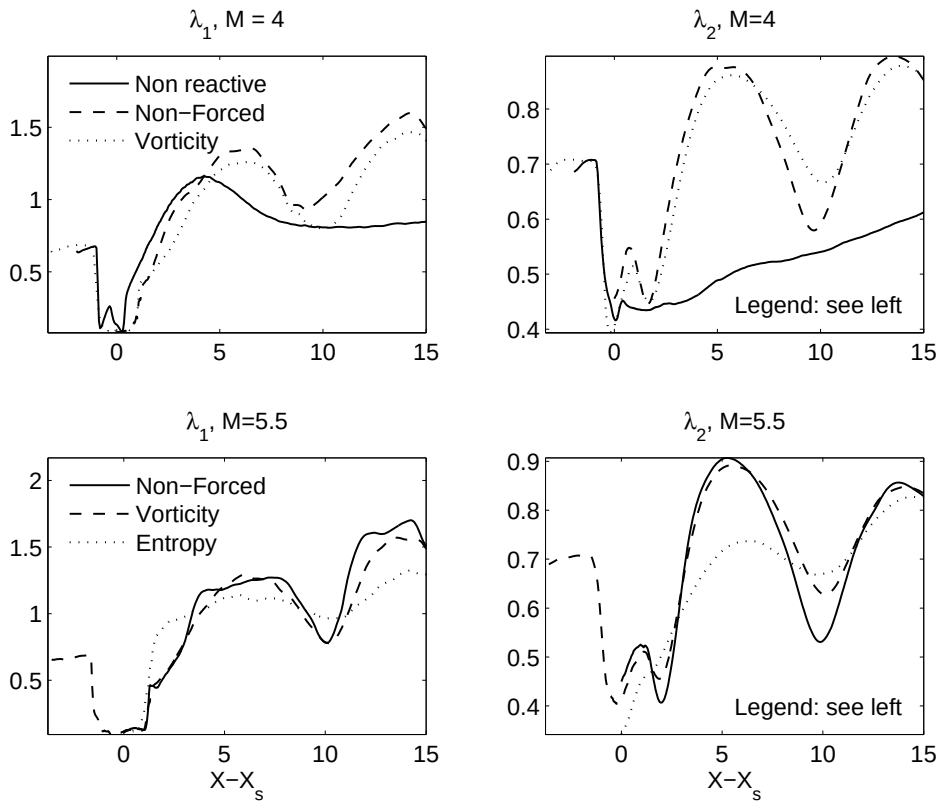

Figure 16. Comparison of longitudinal and transverse velocity Taylor's microscales for both heat release cases. The legend shown in the left panel of each row applies also to the adjacent right panel.

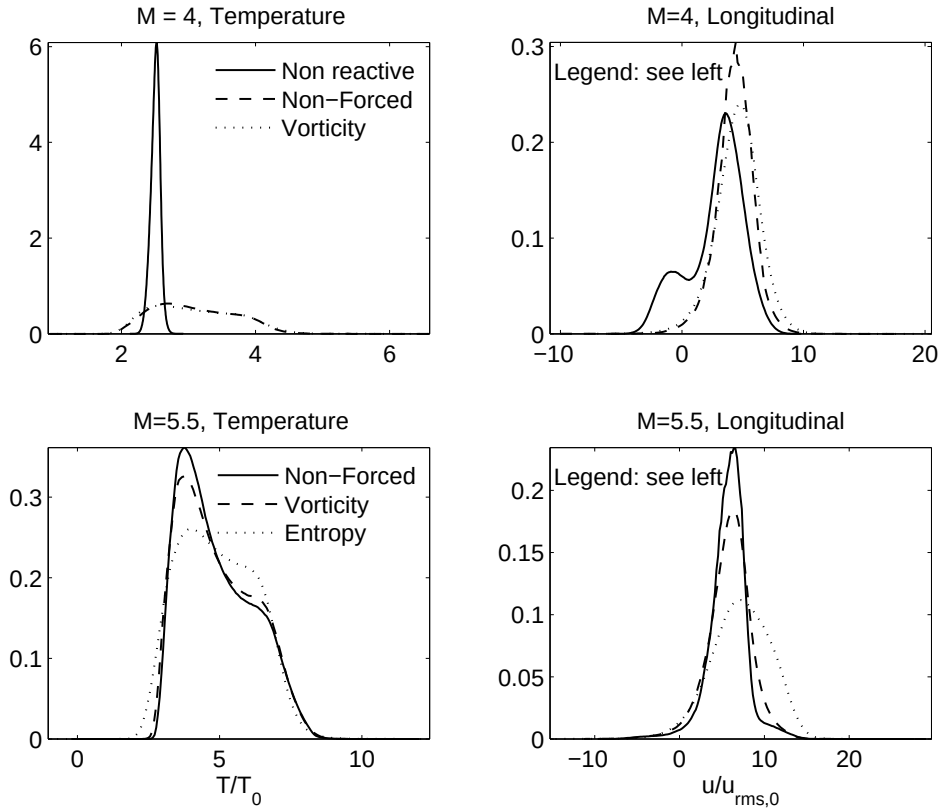

Figure 17. Conditional PDF of temperature and longitudinal velocity for $\lambda < 0.5$ and $p > p_{\mathbf{ZND}}/2$, i.e. , in the reaction zone.

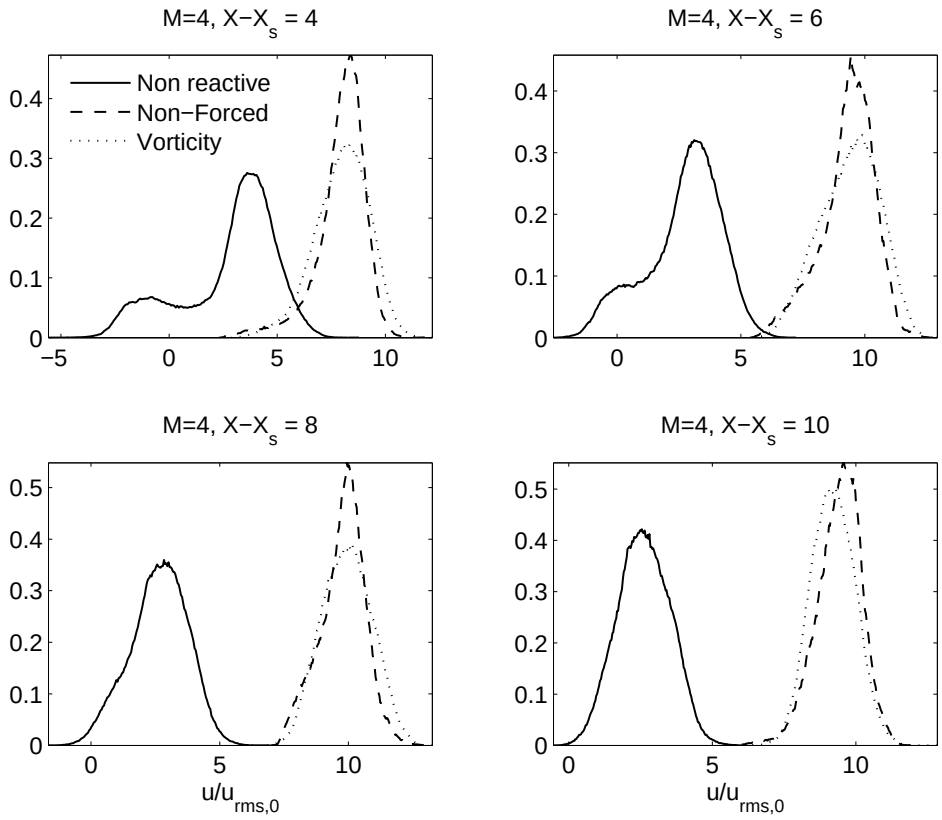

Figure 18. Low heat release longitudinal velocity PDF at constant x, for various distances from the shock. The legend shown in the top-left panel applies to all four panels.

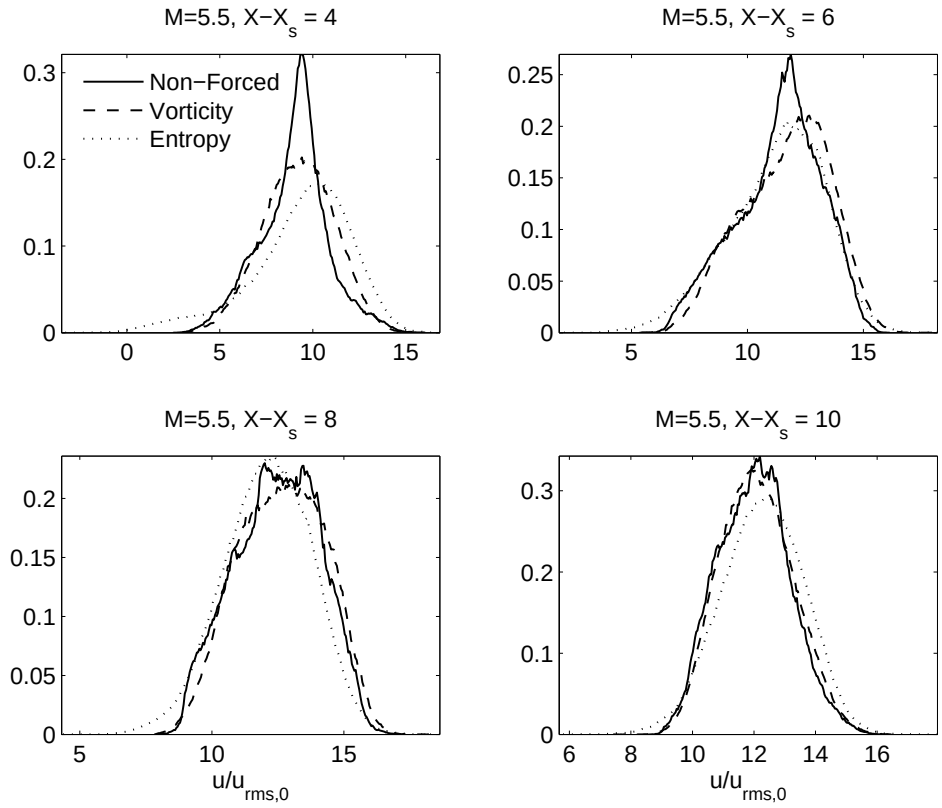

Figure 19. High heat release longitudinal velocity PDF at constant x, for various distances from the shock. The legend shown in the top-left panel applies to all four panels.

0.235, postshock fluctuations in reactive conditions are dominated by wavelengths associated with the natural fluctuations. The introduction of vortical and entropy perturbations reduces, but does not shift, peak intensities in the one-dimensional kinetic energy spectra. Transverse velocity variances are considerably augmented above the unforced value by both vortical and entropic fluctuations. The reactivity in the post-shock region eliminates the peak in longitudinal variance due to the contribution of sub-critical acoustics to velocity components. Both linear and nonlinear analysis agree in this respect.

Integral length scales are markedly increased by natural (limit cycle) oscillations above the nonreactive values. Entropy fluctuations are more effective than vorticity analogs in reducing the integral scales. Taylor microscales based on the velocity components are increased by reactivity, which considerably stretches small structures in the longitudinal direction. Different from the integral length scale case, the addition of pre-shock forcing weakly affects velocity microscales. Probability distribution functions for forced cases manifest a flattened profile when compared to detonations propagating in unperturbed fields.

Both forcing conditions lead to an increased probability of high temperature fluid in the reaction zone. Linear analysis shows the presence of a substantial peak of the temperature variance in the reaction region for high activation energies. It is, therefore, the structure of the reactive region that leads to thermal amplification, and possibly to the formation of hot spots. Entropy forcing leads to the formation of large pockets of unburned material, detached from the shock. These effects are also present in vortical forcing cases, but are of reduced magnitude.

Future work will focus on two aspects of detonation–turbulence interaction. First is the analysis of large activation energies, beyond the longitudinal stability limit. Based on present results, large activation energies are likely to support hot spot formation for strong inflow forcing. Second, large N and Re numbers will be investigated using a large eddy simulation (LES) approach built upon the present DNS effort.

References

[1]G. Ciccarelli and S. Dorofeev. Flame acceleration and transition to detonation in ducts. *Prog. Energy Combust. Sci.* 34:499, (2008).

[2]B.E. Gelfand, S.M. Frolov and M.A. Nettleton. Gaseous detonations. A selective review. *Prog. Energy Combust. Sci.* 17:327-371, (1991).

[3]C.K. Law. Combustion Physics. *Cambridge University Press* (2006).

[4]S.B. Dorofeev, M.S. Kuznetsov, V.I. Alekseev, A.A. Efimenko, and W. Breitung. Effect of scale on the onset of detonations. *Shock Waves* 10:137, (2000).

[5]A.M. Khokhlov, E.S. Oran, A.Y. Chtchelkanova and J.C. Wheeler. Interaction of a shock with a sinusoidally perturbed flame. *Combust. Flame* 117:99, (1999).

[6]F.A. Bykovskii, S.A. Zhdan, and E.F. Vedernikov. Continuous Spin Detonations. *J. Propulsion Power* 22:1204, (2006).

[7]H.S. Ribner. Spectra of Noise and Amplified Turbulence Emanating from Shock–Turbulence Interaction. *AIAA J.* 25(3):436–442, (1987).

[8]S.L. Gavrilyuk and R. Saurel. Estimation of the turbulent energy production across a shock wave. *J. Fluid Mech.* 549:131, (2006).

[9]S. Lee, S.K. Lele, and P. Moin. Interaction of Isotropic Turbulence with Shock Waves: Effect of Shock Strength. *J. Fluid Mech.* 340:225-247, (1997).

[10]S. Jamme, J.B. Cazalbou, F. Torres, and P. Chassaing. Direct numerical simulation of the interaction between a shock wave and various types of isotropic turbulence. *Flow, Turbulence and Combustion* 68:227-268, (2002).

[11]F. Ducros, V. Ferrand, F. Nicoud, C. Weber, D. Darracq, C. Gacherieu, and T. Poinsot. Large eddy simulation of the shock/turbulence interaction. *J. Comp. Phys.* 152:517-549, (1999).

[12]P.S. Rawat and X. Zhong. Numerical Simulation of Shock–Turbulence Interactions using High-Order Shock-Fitting Algorithms. AIAA 2010-114, Orlando, FL, (2010).

[13]J.H. Agui, J. Briassulis and G. Andropoulos. *J. Fluid Mech.* 524:143, (2005).

[14]S. Xanthos, M. Gong and G. Andropoulos. Velocity and vorticity in weakly compressible isotropic turbulence under longitudinal expansive straining. *J. Fluid Mech.* 584:301, (2007).

[15]S. Lee, S.K. Lele, and P. Moin. Simulation of spatially evolving turbulence and the applicability of Taylor's hypothesis in compressible flow. *Phys. Fluids A* 4:1521, (1992).

[16]H.S. Ribner, Convection of a pattern of vorticity through a shock wave, NACA Report 1164, (1954).

[17]T.L. Jackson, M.Y. Hussaini, and H.S. Ribner. Interaction of Turbulence with a Detonation Wave. *Phys. of Fluids A* 5(3):745–749, (1993).

[18]L. Massa and F.K. Lu. Role of the induction zone on turbulence–detonation interaction. AIAA paper number AIAA-2009-3949.

[19]Short and Stewart. Cellular detonation stability. Part 1. A normal mode linear analysis. *J. Fluid Mech.* 368:229-262, (1998).

[20]Texier and Zumbrun. Transition to longitudinal instability of detonation waves is generically associated with Hopf bifurcation to time-periodic galloping solutions. *Submitted. See also: Texier and Zumbrun. Hopf Bifurcation of Viscous Shock Waves in Compressible Gas Dynamics and MHD. Arch. Rational Mech. Anal. 190:107, (2008).*

[21]H.S. Dou, H.M. Tsai, B.C. Khoo, and J. Qiu. Simulations of Detonation Wave Propagation in Rectangular Ducts Using a Three-Dimensional WENO Scheme. *Combust. Flame* 154(4):644–659, (2008).

[22]J.M. Austin. The Role of Instability in Gaseous Detonation. PhD Thesis, California Institute of Technology (2003).

[23]Berthet, Petrossian, Residori , Romand, and Fauve. Effect of multiplicative noise on parametric instabilities. *Physica* 174:84, (2003).

[24]Horsthemke and Lefever. Noise-induced Transitions. Springer, Berlin, (1984).

[25]Gammaitoni, Hanggi, Jung, and Marchesoni. Stochastic resonance. *Rev. Mod. Phys.* 70:223, (1998).

[26]J.O. Hinze. Turbulence, McGraw-Hill, p. 247, (1975).

[27]J.E. Moyal. The spectra of turbulence in a compressible fluid; eddy turbulence and random noise. *Proc. Cam. Phil. Soc.* 48(2):329-344, (1952) .

[28]T.L. Jackson, A.K. Kapila and M.Y. Hussaini. Convection of a pattern of vorticity through a reacting shock wave. *Phys. of Fluids* 2(7):1260-1268, (1990).

[29]L. Massa, M. Chauhan and F.K. Lu. Detonation–Turbulence Interaction. *Under Review.*

[30]L. Massa, J.M. Austin, and T.L. Jackson. Triple point shear-layers in gaseous detonation waves. *J. Fluid Mech.* 586:205, (2007).

[31]M. V. Morkovin. Effects of compressibility on turbulent flows. In Mecanique de la Turbulence (ed. A. Favre), pp. 367–380. Paris, Editions du Centre National de la Recherche Scientifique, (1961).

[32]K. Mahesh, S.K. Lele, and P. Moin. The influence of entropy fluctuations on the interaction of turbulence with a shock wave. *J. Fluid Mech.* 334:353–379, (1997).

[33]Z.U.A. Warsi. Fluid Dynamics. CRC press, (1993).

[34]S.K. Lele and J. Larsson. Shock–Turbulence interaction: What we know and what we can learn from peta-scale simulations. *Journal of Physics: Conference Series* 180:012032, (2009).

[35]P.A. Davidson. Turbulence, An introduction for scientists and engineers. Oxford University Press, pp. 456-468 (2006).

[36]Y.X. Huang, F.G. Schmitt, Z.M. Lu, Y.L. Liu. Autocorrelation function of velocity increments time series in fully developed turbulence. *Europhysics Letters (EPL)* 86:40010, (2009).